JOURNAL OF CATALYSIS 143, 345–368 (1993)

Bimetallic Synergy in Cobalt–Ruthenium Fischer–Tropsch Synthesis Catalysts

ENRIQUE IGLESIA,[1] STUART L. SOLED, ROCCO A. FIATO, AND GRAYSON H. VIA

Corporate Research Laboratories, Exxon Research and Engineering Co., Route 22 East, Annandale, New Jersey 08801

Received February 11, 1993; revised April 30, 1993

The addition of small amounts of Ru to Co/TiO_2 or Co/SiO_2 catalysts (Ru/Co < 0.008 at.) increases their turnover rate and C_5+ selectivity in the Fischer–Tropsch synthesis. Also, deactivated bimetallic Co–Ru catalysts can be regenerated by a hydrogen treatment at reaction temperature whereas monometallic Co catalysts cannot. On Co/TiO_2, Ru addition increases turnover rates by a factor of three and C_5+ selectivities from 84.5 to 91.1%, without an apparent change in cobalt dispersion. Activation energies and reaction kinetics are unaffected by Ru addition. These data suggest that the presence of Ru leads to higher Co site density during reaction without modifying the chemical reactivity of exposed Co surface atoms. Ru appears to inhibit the deactivation of surface Co ensembles. Ru atoms at the surface of Co crystallites increase the rate of removal of carbon and oxygen species during reaction and during regeneration of deactivated Co catalysts. The resulting higher Co site density leads to higher apparent turnover rates and to enhanced readsorption of α-olefins. As a result, Co–Ru catalysts yield a heavier and more paraffinic product than monometallic Co catalysts with similar initial dispersion. The observed bimetallic interactions require intimate contact between Co and Ru, a state that forms during oxidation of the bimetallic precursors at high temperature. This treatment induces migration of Ru oxide species and leads to mixed Co–Ru oxides. The reducibility and the carbon deposition rates on well-mixed bimetallic Co–Ru catalysts are very different from those of monometallic Co catalysts. Electron microscopy, X-ray absorption spectroscopy, and thermogravimetric studies confirm the intimate mixing required for catalytic rate and C_5+ selectivity enhancements, for faster reduction of Co oxide precursor, and for inhibition of carbon deposits during reactions of H_2/CO mixtures.

1. INTRODUCTION

Hydrocarbon synthesis is a crucial step in the conversion of remote natural gas to fuels and petrochemicals. Cobalt-based catalysts are widely used in reactions of CO and H_2 (the Fischer–Tropsch synthesis) (*1–4*) to form linear aliphatic hydrocarbons with a broad molecular weight distribution typical of polymerization processes (*5*). Methane and C_2–C_4 selectivities on Co catalysts are high at temperatures above 523 K, conditions often required for high volumetric reactor productivities. On many cobalt catalysts, metal- and site–time yields are low below 473 K, conditions at which CH_4 selectivities are less than 15% (Table 1). Also, the regeneration of deactivated cobalt catalysts is difficult, often requiring sequential hydrogen and steam treatments or a solvent wash (*1, 2*).

Our previous studies addressed the role of primary and secondary reactions (*6–9*), and of metal dispersion and metal–support interactions (*10*) in the control of hydrocarbon synthesis rate and selectivity. Here, we describe synergistic bimetallic interactions between Co and Ru, which increase Fischer–Tropsch (FT) synthesis rate and C_5+ selectivity on supported cobalt catalysts. Improved activity and selectivity apparently arise from a Ru-promoted cleansing of cobalt surface ensembles during FT synthesis. Ru-catalyzed hydrogenolysis of

[1] Present address: Department of Chemical Engineering, University of California at Berkeley, Berkeley, CA 94720.

0021-9517/93 $5.00

TABLE 1

Fischer-Tropsch Synthesis Rate and Selectivity on Typical Monometallic Cobalt Catalysts

Support	Temperature (K)	Pressure (kPa)	Cobalt-time yield (10^4 s^{-1})	Selectivity (%)		
				CH_4	C_5+	Ref.
$ThO_2 \cdot MgO \cdot$ Kieselguhr	458	100	4.7	12	80	(*37*)
SiO_2	473	100	4.6	—	—	(*38*)
Al_2O_3	488	100	11.6	4	—	(*39*)
TiO_2	498	100	4.7	16	52	(*39*)
$ZrO_2 \cdot SiO_2$	493	2000	26.1	8	88	(*40*)

Note. [$H_2/CO \sim 2$].

carbonaceous residues and reduction of surface oxygen species permits regeneration of these bimetallic catalysts using H_2 at low temperatures (473–503 K).

2. BACKGROUND

2.1. Synergistic Promotion

The notion of "synergy" or synergetic promotion was first used in 1912 by R. Willstätter to describe enzyme-catalyzed reactions in which the total reaction rate on binary enzyme mixtures was greater than the sum of the rates on the two separate enzymes (*11*). In heterogeneous catalysis, synergistic effects may arise from textural or chemical promotion, such as in silica and potassium promotion of Fe-based ammonia synthesis catalysts. Textural promoters, such as SiO_2, increase the number of surface sites in the fresh catalyst. Chemical promoters, such as K, increase the intrinsic activity of surface sites by lowering the activation energy or entropy for a chemical reaction.

A third form of synergistic promotion apparently occurs on Co–Ru catalysts. Small amounts of Ru (Ru/Co < 0.008 at.) improve the activity and selectivity of cobalt catalysts without increasing the initial site density (textural promotion) or changing the site activity and activation parameters (chemical promotion). Carburization studies suggest that this synergistic behavior may arise from inhibited deactivation of cobalt active sites during hydrocarbon synthesis on Co–Ru catalysts. In other words, Ru maintains a higher density of available Co reaction sites. A similar effect may also account for the synergistic effect of Ir in Pt–Ir materials for catalytic reforming (*12*).

2.2. Previous Work

Several patents (*13–16*) disclose bimetallic Co–Ru catalysts supported on ThO_2 and La_2O_3–Al_2O_3 for FT synthesis. The bimetallic catalysts show higher synthesis rates and C_5+ selectivities than monometallic Co catalysts. These reports do not describe any Ru effects on deactivation or regeneration behavior, but find synergistic effects when Co–Ru samples are calcined before reduction (*13, 16*). Metal-time yields and C_5+ selectivities of previously reported Co–Ru/Al_2O_3 catalysts are somewhat lower than those reported here for TiO_2- and SiO_2-supported Co–Ru catalysts (Table 2), but direct comparisons are difficult because of different reaction conditions.

Co–Ru/Al_2O_3 catalysts prepared from Ru(III) hexacyanocobaltate have been used for methanation reactions (*17*). Mixed molten salts of Co and Ru also catalyze the synthesis of alcohols from CO/H_2 mixtures (*18*).

3. EXPERIMENTAL

3.1. Catalyst Synthesis

TiO_2-supported cobalt catalysts were prepared by incipient wetness impregnation of

TABLE 2

Fischer–Tropsch Synthesis on Cobalt–Ruthenium Bimetallic Catalysts (*14*)

Catalyst	Pressure (KPa)	Temperature (K)	CO conversion (%)	Co-time yield (10^4 s^{-1})	CH_4 (%)	C_5+ (%)	CO_2 (%)
A	100	468	30	0.83	10	79	2
A	200	468	14	1.1	15	73	2
A	200	478	27	1.9	19	64	2
A	200	488	35	2.5	22	58	2
A	500[b]	473[b]	—	1.7	~20[b]	~60[b]	~2[b]
B	1500	468	—	12.5	—	—	—
$CoRu/TiO_2$[a] (calcined)	500	473	25.3	8.1	7.5	86.7	0.2
	2000	473	61.0	13.1	5.0	91.1	0.1
$CoRu/SiO_2$[a]	2000	473	63.0	8.4	5.8	86.1	0.1

Note. Catalysts: (A) $Co/Ru/ThO_2/Al_2O_3$ (21.9/0.5/2.2/75.4 wt.); H_2/CO = 2/1, from data in Refs. (*14*, *15*). (B) $Co/Ru/La_2O_3/Al_2O_3$ (20.0/0.10/1.0/78.9); H_2/CO = 2/1, from data in Ref. (*13*).

[a] Catalysts of our study.

[b] Extrapolated to the conditions of our study using temperature and pressure dependence reported in Ref. (*14*).

Degusa P25 TiO_2 (70% rutile, 35 m^2 g^{-1}, calcined at 833 K for 4 h) with an aqueous solution of $Co(NO_3)_2 \cdot 6H_2O$ (Alpha, Puratronic Grade) in doubly distilled deionized water (*19*, *20*). Impregnation was carried out in two stages, with air-drying at 373 K between them. The catalyst was calcined at 673 K in air for 4–5 h, reduced in flowing H_2 at 673 K for 16 h, and passivated using a dilute oxygen stream (1% O_2/He). The cobalt content was 11.6% wt.

Co–Ru/TiO_2 catalysts were prepared by adding a Ru nitrate (Engelhard)/acetone solution to an acetone slurry containing the pretreated Co/TiO_2 catalyst, followed by evaporation of the acetone solvent while stirring. The cobalt and ruthenium contents were 11.6 and 0.14% wt., respectively, corresponding to an atomic Ru/Co ratio of about 0.0067. A portion of this catalyst was reduced in H_2 at 673 K for 16 h, while the remaining part was calcined in 20% O_2/He at 573 K for 4 h before a similar reduction treatment. Other Co–Ru/TiO_2 catalysts were similarly prepared from the same Co/TiO_2 precursor but with different Co/Ru ratios (0.001–0.014 at.).

SiO_2-supported cobalt was prepared by incipient wetness impregnation of Davison 62 SiO_2 (280 m^2 g^{-1}, calcined at 873 K for 16 h) with an aqueous solution of Co $(NO_3)_2 \cdot 6H_2O$ (Alfa, Puratronic Grade) in doubly distilled deionized water. Impregnation was carried out in four stages with air-drying at 373 K between them. The catalyst was then calcined in 20% O_2/He at 673 K for 4 h, reduced in flowing H_2 at 673 K for 16 h, and passivated. The cobalt content was 23.0% wt.

The bimetallic Co–Ru/SiO_2 catalyst was prepared from this Co/SiO_2 using the synthesis and pretreatment procedures described above for TiO_2-supported catalysts. Cobalt and ruthenium contents were 23.0 and 0.26% wt., respectively, corresponding to an atomic Ru/Co ratio of about 0.0070.

3.2. Thermogravimetric Analysis

A thermal balance (Mettler TA 2000 C) was used to measure weight changes (TG) and rates of weight change (DTG) in flowing H_2 or 1 : 1 H_2/CO mixtures at atmospheric pressure. Peaks in the derivative curve (DTG) correspond to maximum rates in

weight change. Gas flows (1.67 cm^3 s^{-1}), catalyst charges (0.15 g), and heating rates (0.1 K s^{-1}) were kept constant in all experiments. All samples were reduced in H_2 from room temperature to 773 K. After the H_2 treatment, the sample was cooled and treated in a 1 : 1 H_2/CO mixture. Carbon growth rates were then obtained from the rate of weight change in H_2/CO mixtures. X-ray diffraction spectra before and after thermogravimetric experiments confirmed the identity of the solid phases suggested by the observed changes in sample weight.

3.3. Electron Microscopy

Electron microscopy studies were conducted in a Philips EM-420ST high-resolution transmission electron microscope with scanning transmission and energy dispersive X-ray analysis capabilities and a resolution of about 0.25 nm. The catalyst samples were ground and ultrasonically dispersed in butyl alcohol. A drop of the suspension was then air-dried on a porous carbon film (*21*).

Elemental analysis of individual Co and Co–Ru crystallites was performed using an attached energy dispersive X-ray analyzer (PGT, System 4) and a 1-nm beam. At these conditions, particles as small as 1 nm could be analyzed with X-ray spatial resolutions of 0.25 nm and a detectability limit for Co and Ru of about 0.25% wt. in the sampled volume.

3.4. X-Ray Absorption Measurements

The oxidation state and the local chemical environment of Ru atoms in Co–Ru catalysts was examined by X-ray absorption fine structure (XAFS) measurements at the Ru *K*-edge (22117 eV). XAFS data were obtained on beam line 6-2 at the Stanford Synchrotron Radiation Laboratory using a Si(220) crystal monochromator in the unfocused mode. The electron storage ring energy was 3 GeV during experiments and the beam line wiggler was operated at 8.5 kG field strength.

A TiO_2-supported Co–Ru sample containing 0.14% wt. Ru and 11.6% wt. Co was used in all experiments. X-ray absorption spectra were obtained on samples directly reduced in flowing dihydrogen at 773 K after Ru impregnation or calcined at various temperatures (473, 623, or 773 K) before reduction in dihydrogen. In each case, the material (1 g) was pressed into a self-supporting pellet of 3.1 cm diameter and placed within a heated cell designed to collect transmission and fluorescence XAFS data while keeping samples within a controlled environment (temperature and gas composition) (*22*). Data were collected with a fluorescence detector (*23*) using Kr as the detector gas. The ratio of fluorescence to scattered incident beam radiation was enhanced using a three-absorption length Mo filter.

After mounting the sample pellet, the cell was flushed with He to remove any remaining air and the temperature was increased from room temperature to 800 K at 0.33 K s^{-1}. Dihydrogen (1.66 cm^3 s^{-1}) was then introduced into the cell and the temperature was kept at 800 K for 1 h. The sample was cooled to 130 K using liquid nitrogen and the XAFS data collected at these conditions in flowing dihydrogen.

After XAFS data were collected, these reduced samples were flushed with He while warming to room temperature and then exposed to an oxygen-containing stream (20% O_2/He) for 0.25 h. This treatment causes oxygen to chemisorb on metal atoms exposed at the surface of crystallites in the samples. The flowing gas was then again switched to He and XAFS data were collected at 130 K.

The local chemical environment (backscatterer identity, coordination numbers, radial distances, disorder parameters) of Ru atoms in reduced Co–Ru samples was described using mathematical procedures reported in previous publications (*24, 25*). Radial structure functions were obtained by Fourier transforms of EXAFS data between 2.5 and 17 $Å^{-1}$ wavenumbers; the region between 1 and 3 Å was Fourier-filtered in order to isolate the components of the first coordination sphere surrounding Ru scatter-

ers. These data were then fitted over the 3–14 $Å^{-1}$ range using experimental amplitude functions for Ru and Co scatterers, experimental phase functions for Ru–Ru species, and a theoretical phase function (*26*) for Ru–Co bonds. Reference data for the experimental amplitude and phase functions were obtained from transmission XAFS data on the pure metals at 100 K. The fitting function contained seven parameters: the average number of Co and Ru atoms in the first Ru coordination sphere, the Ru–Ru and Ru–Co bond distances, the mean square deviation for each interatomic distance, and a phase shift parameter, ΔE_0, for the theoretical Ru–Co phase function.

The Ru edge XAFS spectra in samples exposed to oxygen at RT after reduction differ from those in reduced samples, suggesting that a significant fraction of the Ru atoms is available at crystallite surfaces and chemisorbs oxygen. The resulting analysis of the oxygen content within the first Ru coordination sphere provides only an indirect measure of exposed Ru because corrosive chemisorption, surface segregation, and bulk oxidation can occur at RT, especially on highly dispersed particles. The models and procedures used to describe the coordination sphere of Ru in oxygen-exposed samples was similar to that described for the reduced catalysts. In this case, a third reference spectrum (RuO_2) is required in order to account for the contributions of Ru–O bonds to the EXAFS spectra. The required amplitude and phase functions are obtained from experimental spectra of RuO_2. The fitting procedure includes two additional parameters: the number and interatomic distance of Ru–O bonds in the first Ru coordination sphere.

3.5. *Characterization Methods*

Dihydrogen uptakes were measured in an all-glass static chemisorption unit pumped by diffusion and mechanical pumps isolated from the system by liquid-nitrogen traps (dynamic vacuum $< 10^{-5}$ Pa). Pre-reduced and passivated samples were reduced again in hydrogen (3.3 cm^3 H_2/g^{-1} s^{-1}) for 1–2 h at various temperatures, and then evacuated to less than 10^{-4} Pa for 0.5–1.0 h at temperatures above those required to remove all chemisorbed hydrogen (>523 K). The samples were then cooled to 373 K and isotherms measured at three to five H_2 pressures between 13 and 80 kPa. Adsorption isotherms were extrapolated to zero pressure to obtain chemisorption uptakes. Dispersion values were calculated from the hydrogen uptake and the cobalt content of the catalysts assuming a 1 : 1 stoichiometry of H to surface cobalt atoms.

X-ray diffraction patterns were measured in a Philips 3000 APD diffractometer using Cu-$K\alpha$ radiation and a scintillation detector. Metal and oxide crystallite sizes were obtained from the line width of the most intense reflections using the Scherrer equation (*27*). Cobalt contents were measured by X-ray fluorescence and ruthenium contents by atomic absorption. Catalyst surface areas and pore size distributions were measured by dinitrogen physisorption using the BET and Kelvin isotherms, respectively.

3.6. *Catalytic Measurements*

Catalytic properties of Co and Co–Ru samples were measured in an isothermal (±1 K) plug-flow tubular reactor (453–503 K, 100–2050 kPa, $H_2:CO = 2.05:1$, 2–10 g catalyst sample). Samples were reduced in H_2 at 573–973 K, cooled to synthesis temperatures, and exposed to H_2/CO reactants. All reported data were measured after 24–48 h on stream in order to ensure steady-state behavior. Site–time yields were measured on catalyst pellets with average diameters less than 0.2 mm in order to avoid diffusion-limited reactant conversion at catalytic sites.

C_1–C_{15} hydrocarbons and CO, H_2, CO_2, and N_2 were analyzed on-line by capillary and packed column chromatography using thermal conductivity, flame ionization, and mass spectrometric detection (*6*). N_2 was used as an unreactive internal standard to ensure accurate mass balances. $C_{16}+$ hy-

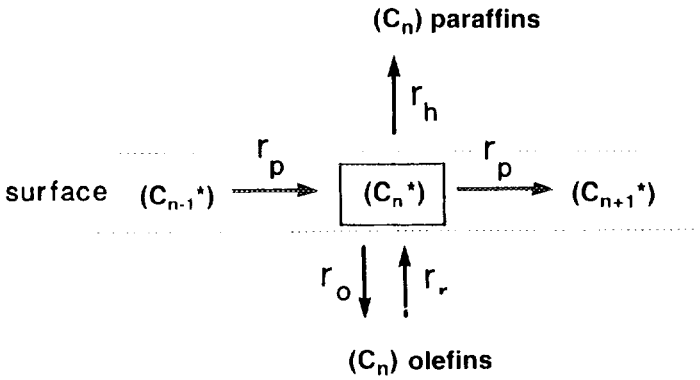

SCHEME 1

drocarbons were collected and their composition determined by high-temperature gas and gel-permeation chromatography (*6*, *7*).

Reactant mixtures ($H_2:CO:N_2 = 61:31:8$) were prepared from Matheson feedstocks (UHP grade) and purified by passing over a Pd/Al_2O_3 catalyst (Johnson–Mathey), an activated charcoal bed, and a molecular sieve (13X) trap, all held at ambient temperature, in order to remove O_2, H_2O, and metal (Ni, Fe) carbonyl impurities.

Hydrocarbon synthesis rates are reported normalized to the total cobalt content (*cobalt–time yields*, defined as the moles of CO converted per unit time per g-atom Co) or to the number of Co surface atoms (*site–time yields*, defined as the molecules of CO converted per unit time per surface Co atom). Hydrocarbon selectivities are reported on a carbon-atom basis as the percentage of the converted CO appearing as a given hydrocarbon product.

Hexadecane hydrogenolysis rates and selectivities were measured in a semicontinuous stirred tank reactor containing liquid hexadecane and about 1 g of catalyst under stirring intensities that avoid mass transfer limitations. Hydrogenolysis site–time yields were defined as the number of moles of carbon atoms appearing in the products per surface metal atom per s. Product analysis was carried out by on-line capillary column gas chromatography using a flame ionization detector.

3.7. Product Distributions in the Fischer–Tropsch Synthesis

Kinetic formulations developed for polymerization processes are commonly used to describe product distributions in the Fischer—Tropsch synthesis, a modified polymerization reaction using adsorbed carbon species (CH_x from CO) as monomers (Scheme 1). The Flory equation predicts carbon number distributions that obey the equation (*5*, *28*)

$$S_n = n \cdot (1 - \alpha)^2 \cdot \alpha^{n-1},$$

where S_n is the carbon selectivity for chains with n carbon atoms, when the chain growth probability,

$$\alpha = \frac{r_p}{r_p + r_t}$$

is independent of carbon number (n). A plot of $\ln (S_n/n)$ vs n gives a straight line when α is independent of chain size.

A more general treatment allows for chain growth kinetics that depend on chain size. In this approach, the termination probability for a given chain size is calculated using (*29*)

$$\beta_n = \frac{r_{t,n}}{r_{p,n}} = \left(1 - \frac{1}{\alpha_n}\right) = \frac{\phi_n}{\sum_{i=n+1}^{\infty} \phi_i},$$

where ϕ_n is the mole fraction of chains of size n, and $r_{t,n}$ and $r_{p,n}$ are their chain termination and propagation rates, respectively. The denominator in this equation requires that we accurately measure the entire product distribution. The chain termination probability is a linear combination of the net values for each termination step; these net values include the rates of both forward and reverse steps. For example, if chains terminate to paraffins ($\beta_{h,n}$) and olefins ($\beta_{0,n}$) and the latter readsorb and initiate surface chains ($\beta_{r,n}$), the total chain termination probability is given by

$$\beta_{T,n} = \beta_{h,n} + (\beta_{0,n} - \beta_{r,n}).$$

4. CHARACTERIZATION OF BIMETALLIC COBALT CATALYSTS

4.1. Thermogravimetric Analysis

The effect of Ru on the reduction and carburization properties of Co/TiO_2 samples (11.6% wt. Co; 0.03, 0.07, and 0.15% wt. Ru) was examined by thermogravimetric measurements in H_2 or H_2/CO streams. We observe two significant differences between Co/TiO_2 and $Co–Ru/TiO_2$ samples; these differences are most striking if Co–Ru catalysts are calcined in air at 673 K after impregnating with Ru. First, the onset of reduction occurs at lower temperature ($\Delta T = -50$ K) on Ru-containing samples (Fig. 1). Also, carbon forms rapidly from H_2/CO reactants on Co/TiO_2 samples above 623 K, but not on $CoRu/TiO_2$ even above 773 K (Fig. 2). These two effects, the more rapid reduction of Co_3O_4 to Co metal and the inhibition of carbon deposits from CO/H_2 mixtures, are strong indicators of intimate contact between Co and Ru components and of strong bimetallic effects. As we discuss below, this contact is strengthened by the surface migration of metal oxides, a process that occurs during the calcination treatment.

Co_3O_4/TiO_2 precursors reduce to supported metal crystallites in two steps that lead to distinct peaks in DTG plots (Fig. 1). In the first step, Co_3O_4 reduces to CoO; this

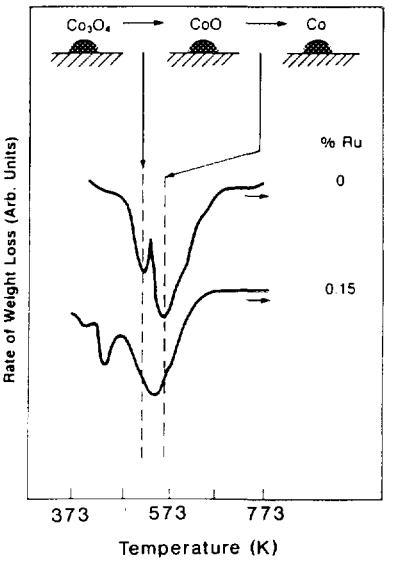

FIG. 1. The effect of Ru on the reduction of Co_3O_4/TiO_2 precursors (11.6% wt. Co, 0.14% wt. Ru).

step is influenced strongly by the presence of very small amounts of Ru (atomic Ru/Co = 0.0067). In the second step, CoO (Co^{+2}) reduces to Co in a broader peak, which occurs at higher temperature and appears to respond more weakly to the presence of Ru (Fig. 1). The reaction stoichiometry obtained from the peak areas in Fig. 1 and the X-ray diffraction spectra of samples before and after reduction and at intermediate stages of reduction confirm the proposed reduction sequence. At the low Ru levels in our samples, we are unable to detect the presence of Ru, either as a distinct reduction peak in DTG spectra or as a reflection line in X-ray diffraction patterns.

All reduced Co samples chemisorb CO (from H_2/CO mixtures) near room temperature. Additional CO chemisorbs between 423 and 523 K, leading to the slight weight gain observed in TG spectra (Fig. 2). Some of the chemisorbed CO desorbs above 673 K. Above 673 K, carbon growth occurs rapidly on Co/TiO_2 samples and deposits the equivalent of 100–150 carbon monolayers on available surface cobalt atoms in about 1 h (Fig. 2). These processes lead to fila-

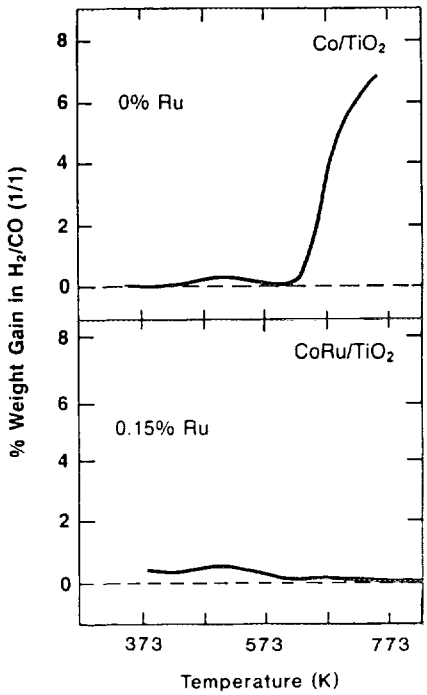

FIG. 2. The effect of Ru on the carburization of Co/TiO_2 and $Co-Ru/TiO_2$ (calcined) in H_2/CO mixtures (H_2/CO = 1/1).

mentous carbon, consisting of whiskers of about 40 nm diameter and containing Co particles at the end away from the support surface. These carbon filaments are clearly seen in our transmission electron micrographs of Co/TiO_2 samples treated in H_2/CO mixtures at 723 K, but not on $Co-Ru/TiO_2$ catalysts treated similarly. Similar types of carbon form during reactions of hydrocarbons on supported Group VIII metals (*30*).

$Co-Ru/TiO_2$ samples with lower Ru contents (0.07% Ru, Ru/Co = 0.0033) require more severe calcination treatments for intimate contact between the two metal components (Fig. 3). Reduction and carburization rates (on Co–Ru samples calcined at 673 K) are similar to those on monometallic Co/TiO_2 samples. After calcination at 773–823 K, however, Co–Ru catalysts reduce at lower temperatures in H_2 and no longer form carbonaceous deposits in H_2/CO mixtures (Fig. 3). Apparently, more extensive migration of metal oxides and better mixing between the two components are required to induce this synergistic behavior as we decrease the Ru content in bimetallic Co–Ru catalysts. At even lower Ru concentrations (0.03% wt. Ru, Ru/Co = 0.0014), reduction and carburization rates are identical to those on Co/TiO_2, even after calcination treatments at 673–823 K.

Ru also increases the rate of reduction of Co_3O_4 supported on SiO_2 (Fig. 4). As on TiO_2-supported samples, calcination of bimetallic precursors enhances Co–Ru interactions. Co/SiO_2 reduces in two steps and the intermediate formation of a CoO phase is clearly detected by X-ray diffraction. In contrast, calcined $Co-Ru/SiO_2$ samples appear to reduce in a single step, possibly because the individual reduction peaks broaden or because a different reduction mechanism occurs on mixed Co–Ru oxides. It appears that intimate Co–Ru contact is more easily achieved on SiO_2 than on TiO_2, consistent with the weaker interactions between metal oxides and SiO_2 and with the higher oxide mobility expected on SiO_2 supports.

The growth of carbonaceous deposits above 673 K depends strongly on the Ru

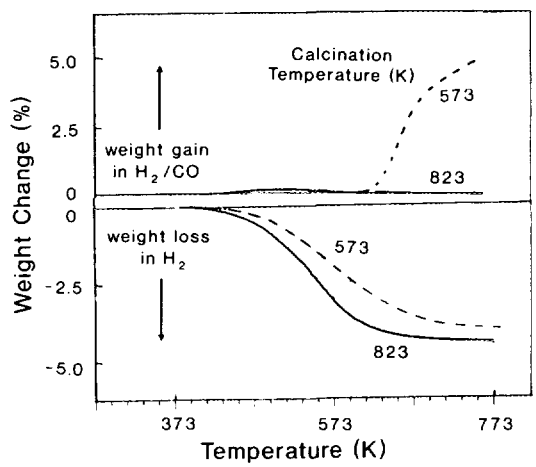

FIG. 3. Effect of calcination temperature on the reduction and carburization of $Co-Ru/TiO_2$ (11.6% Co, 0.07% Ru).

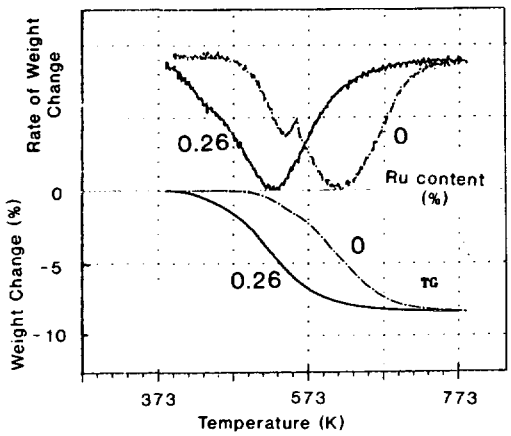

FIG. 4. Ru effects on the reduction of Co/SiO_2 in H_2 (23% wt. Co, 0.26% wt. Ru, 673 K calcination).

concentration and on the calcination temperature. These surprising effects of very small Ru concentrations suggest that enhanced reduction of Co_3O_4 and the inhibition of carbon deposition reactions are very sensitive probes of bimetallic interactions between noble and base members of the Group VIII metals.

We suggest that oxidation treatments enhance interactions between Co and Ru because intimate contact is induced by the higher mobility of Ru oxides and by the formation of stable Co–Ru oxides. In fact, Co_2RuO_4 forms a spinel isostructural with Co_3O_4 (*31*). Consequently, solid solutions of the type $Co_{3-x}Ru_xO_4$, where $0 < x < 1$, can form at least on the surface of Co_3O_4 crystallites during calcination. Reduction of the mixed Co–Ru oxides then leads to intimate bimetallic contact in reduced crystallites. Uncalcined $CoRu/TiO_2$ behaves similar to Co/TiO_2, suggesting that the intimate Co–Ru contact that occurs during calcination is required for enhanced reduction and for inhibited carbon deposition.

4.2. *Electron Microscopy*

The structures of cobalt and cobalt-ruthenium crystallites supported on TiO_2 were examined by transmission electron microscopy. Crystallites are dispersed on titania as slightly elliptical particles about 20–50 nm in size. The diameter of these particles was not affected by calcination at 673 K.

Figure 5 is a typical transmission electron micrograph of a $Co–Ru/TiO_2$ sample calcined at 673 K and reduced in hydrogen before analysis. The three dark regions indicated by the letter "c" in the figure are metal particles, predominantly Co. Elemental analysis of the metal particles show that after calcination–reduction treatments, Ru appears only along with Co within the large metal particles (Fig. 6). Any Ru present within other areas of the support is below the detectability limit (0.25% wt.). The detection of Ru within Co crystallites suggests that Ru selectively deposits on such crystallites and that its distribution throughout the support is nonuniform, at least after calcination at 673 K and reduction in hydrogen.

On Co–Ru samples not calcined before reduction, Ru is not detected within Co crystallites, suggesting that it is more uniformly distributed throughout the support than on calcined samples and that its concentration within Co particles is below 0.25% wt. Therefore, the Ru/Co ratio within such crystallites is below 0.00015, much lower than the bulk value in the sample (0.0067). Crystallite size distributions measured from calcined and uncalcined Co and Co–Ru samples show that neither the presence of Ru nor calcination treatments below 700 K influence the diameter or the shape of the metal crystallites on titania supports (Table 3).

4.3. *X-Ray Absorption Spectroscopy*

Near edge (NEXAFS) and extended fine structure (EXAFS) X-ray absorption spectra were measured at the Ru absorption energy in order to establish the oxidation state and the identity of coordinating atoms around Ru atoms in oxidized and reduced Co–Ru samples.

EXAFS radial distribution functions of reduced Co–Ru samples calcined at various

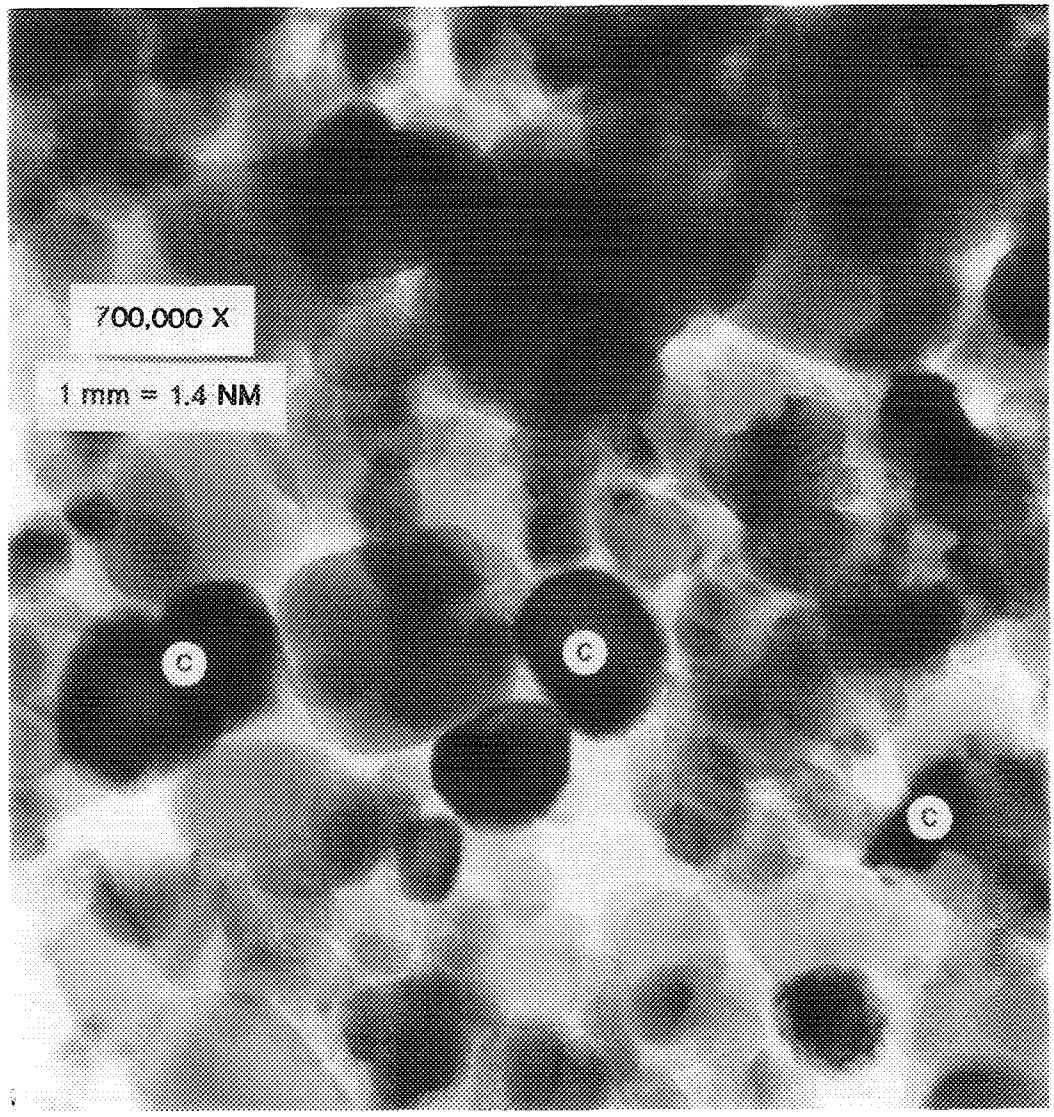

FIG. 5. Transmission electron micrograph of Co–Ru/TiO_2 sample (700,000× magnification; 1 mm = 1.4 nm; 11.6% wt. Co, 0.14% wt. Ru, 673 K calcination).

temperatures before reduction show a decrease in Ru–Ru coordination with increasing calcination temperature (Fig. 7, Table 4). The intensity of the Ru–Ru peak (Fig. 7) decreases, while a peak at 2.02 Å, absent in pure Ru samples and apparently corresponding to Co nearest neighbors ($RuCo_{12}$, Fig. 8), becomes more intense with increasing calcination treatment. A peak at about 3.9 Å also increases; it apparently corresponds to Co next nearest neighbors within bimetallic Co–Ru crystallites. Clearly, calcination treatments enhance the mixing between the two metal components. The fresh uncalcined sample resembles monometallic Ru particles after reduction but Ru atoms

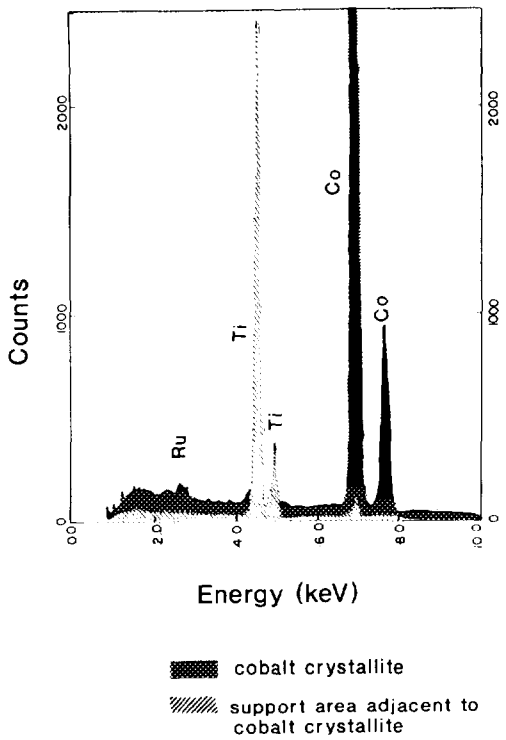

FIG. 6. Elemental analysis of Co–Ru/TiO_2 (calcined) in the TEM. Comparison of regions within and near cobalt crystallite (11.6% wt. Co, 0.14% wt. Ru, 673 K calcination).

quickly acquire an increasing number of nearest neighbors in reduced samples as calcination temperature increases (Table 4).

The fraction of the Ru neighbors consisting of Co atoms in reduced samples can also be calculated from the EXAFS data. The Co fraction in the first Ru coordination shell increases from about 0.3 to about 0.48 as the calcination temperature increases from room temperature (air-exposed sample) to 773 K. This improved mixing occurs along with the apparent agglomeration of the Ru particles, a process that increases the total number of nearest neighbors in the first Ru coordination sphere. Thus, it appears that more intimate mixing occurs by migration of Ru oxide species during calcination; in contrast, the dispersion of the large Co particles is apparently unaffected by calcination, as shown by the similar hydrogen chemisorption uptakes and TEM crystallite sizes in calcined and uncalcined samples (Table 3).

The average Co coordination around Ru atoms underestimates the intensity of the bimetallic mixing because it averages the contributions of any remaining Ru crystallites (containing only Ru–Ru bonds) with those of bimetallic particles. For example, the observed Co fraction around Ru after 773 K calcination (0.48, see Table 4) may well correspond to an equal distribution of Ru between pure Ru and bimetallic crystallites.

The total coordination number of Ru atoms increases with increasing calcination temperature (Table 4), suggesting that sintering of Ru crystallites occurs concurrently with the mixing process. It appears that the mobility induced by forming oxidized Ru species at high temperatures leads to bimetallic mixing and also to sintering during calcination. Interestingly, most of the increase in total coordination number occurs because Ru acquires additional Co neighbors (2.9 to 5.9) and not because of increasing coordination Ru–Ru coordination (6.0 to 6.3) in larger Ru particles.

EXAFS analysis of Co–Ru samples exposed to oxygen at RT after reduction shows that the ability of Ru to chemisorb oxygen is impaired by previous calcination at high temperatures, apparently because a smaller fraction of those Ru atoms are exposed at crystallite surfaces (Table 4). The oxygen fraction in the first coordination sphere decreases from 0.26 to 0.11 when samples are calcined at 773 K. These values cannot be taken as a direct measure of exposed Ru because of concurrent corrosive chemisorption, Co surface segregation, and bulk oxidation processes. These data, however, suggest that some Ru disappears from near-surface regions during calcination; at least some of it migrates into large Co crystallites, suggesting a finite miscibility between Co and Ru at low Ru concentrations. A large fraction of the Ru remains exposed after calcination, suggesting that Co–Ru particles

TABLE 3

Dispersion and Crystallite Size Measurements on Supported Co and Co–Ru Catalysts

	Percent dispersion		Average cobalt particle diameter (nm)[a]		
	523 K Reduction	723 K Reduction	Chemisorption	XRD	TEM
11.6% Co/TiO_2	2.2	0.8	43	>35	36
11.6% Co/0.14% Ru/TiO_2 (calcined)	2.6	0.9	37	>35	—
11.6% Co/0.14% Ru/TiO_2 (reduced)	2.4	0.8	40	>35	34
23% Co/SiO_2	—	3.1	30	25	28
23% Co/0.26% Ru/SiO_2	—	3.3	28	—	—

[a] Using chemisorption uptake after 523 K reduction on TiO_2-supported catalysts; on SiO_2 supports, uptakes after 523 K and 723 K reductions are very similar; diameters calculated from $d/\text{nm} = 96/D$, (D = dispersion), which assumes hemispherical crystallites with random surface orientation exposing low-index crystal planes.

prefer a configuration where most of the Ru in reduced samples lies near outer crystallite surfaces. This proposal is consistent with the X-ray photoelectron data shown in the Appendix.

Our XAFS data clearly show that oxidative treatments above 600 K are required in order to mix the metallic components in Co–Ru/TiO_2 catalysts. These results illustrate the unique ability of X-ray absorption techniques to describe the chemical state and the local environment of minority elements in catalyst samples, under reaction conditions, if required.

4.4. Hydrogen Chemisorption

The cobalt dispersion and the crystallite size measured by hydrogen chemisorption, X-ray diffraction line broadening, and transmission electron microscopy are reported in Table 3. The three methods for estimating cobalt crystallite size are in excellent agreement. The addition of small amounts of Ru to Co/TiO_2 (Ru/Co = 0.0067 at.) and Co/SiO_2 (Ru/Co = 0.0070 at.) does not significantly alter hydrogen chemisorption uptakes at 373 K (Table 3). This result is not surprising because Ru is added as a minor component to a preformed Co catalysts that already contains large (>20 nm) and stable metal crystallites.

Strong metal–support interactions (SMSI) (*32*) in Co/TiO_2 samples cause a strong decrease in hydrogen chemisorption uptakes as reduction temperature increases above 523 K, without an apparent increase in Co crystallite diameter. These interactions are not affected by the presence of Ru and occur with similar intensity on both Co and Co–Ru samples. These interactions do not occur on SiO_2-supported Co catalysts (Table 3). The strength of these SMSI effects can be estimated by comparing chemisorption uptakes after 523 and 723 K. The ratio of these two uptakes is 2.5–3.5 for TiO_2-supported Co and Co–Ru samples, but less than 1.2 for SiO_2-supported Co.

The addition of Ru can increase the apparent dispersion of partially reduced Co catalysts by promoting their more complete reduction during hydrogen treatment. For example, catalysts samples prepared by impregnation of silica with cobalt glycol citrate precursors form a highly dispersed and stable CoO phase, but a hydrogen reduction treatment leads to very low apparent dispersions (1.4%) because of slow reduction even above 773 K (*33*). The addition of Ru (Ru/

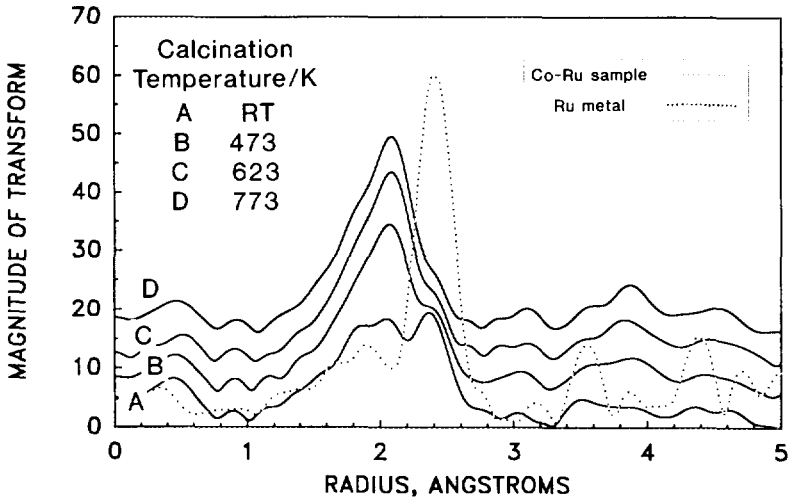

FIG. 7. Radial distribution functions for Co–Ru/TiO_2 catalysts calcined at various temperatures and reduced at 773 K before experiments (Ru *K*-edge: dashed line, monometallic Ru catalyst; solid lines, Co–Ru/TiO_2, 11.6% wt. Co, 0.14% wt. Ru].

Co = 0.0086 at.) increases the apparent Co dispersion to 4.8%, without any apparent change in Co metal crystallite size. Thermogravimetric studies of the reduction process show that this increased metal dispersion reflects the enhanced reduction of the CoO phase in the presence of Ru (*33*). These partially reduced catalysts are not discussed below. In this report, we only include catalysts that are completely reduced (≥95%,

TABLE 4

Composition of First Coordination Sphere of Ru Atoms in Co–Ru/TiO_2 Samples (11.6% wt. Co, 0.14% wt. Ru)

	Calcination temperature (K)			
	RT	473	623	773
	Reduced catalysts			
Coordination number				
N (Ru–Ru)	6.0	7.9	6.8	6.3
N (Ru–Co)	2.9	5.1	5.7	5.9
N (Total)	8.9	13.0	12.5	12.2
Co fraction	0.33	0.39	0.46	0.48
Interatomic distance (nm)				
R (Ru–Ru)	0.268	0.267	0.267	0.268
R (Ru–Co)	0.249	0.252	0.252	0.251
	Catalysts exposed to oxygen (RT) after reduction			
Coordination number				
N (Ru–Ru)	3.2	6.0	6.4	5.0
N (Ru–Co)	2.4	3.3	3.6	4.4
N (Ru–O)	2.0	1.6	1.4	1.2
N (Total)	7.6	10.9	11.4	10.6
Oxygen fraction	0.26	0.15	0.12	0.11

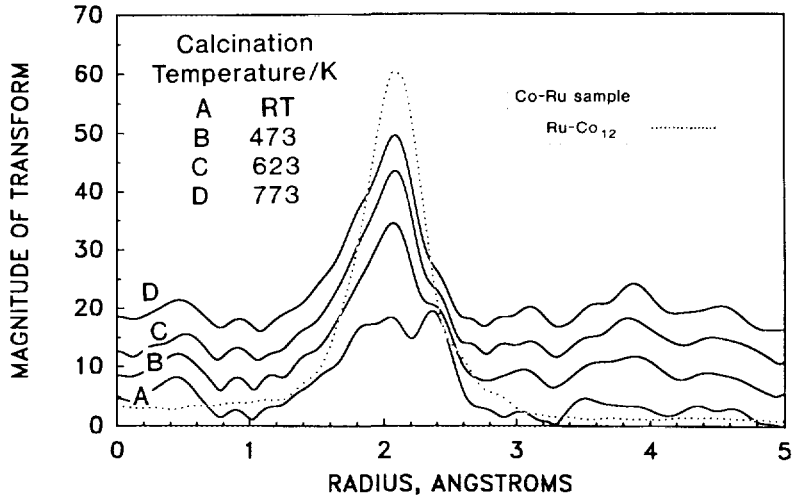

FIG. 8. Radial distribution functions for Co–Ru/TiO_2 catalysts calcined at various temperatures and reduced at 773 K before experiments (Ru *K*-edge: dashed line, monometallic Ru catalyst with Ru surrounded by 12 Co atoms).

by oxygen uptake measurements (*10, 34*)), even in the absence of the Ru component.

5. FISCHER–TROPSCH SYNTHESIS ON Co AND Co–Ru CATALYSTS

5.1. Dispersion and Support Effects on Reaction Rates

Fischer–Tropsch synthesis rates (metal–time yields) are proportional to the number of metal surface atoms exposed at the surface of Co crystallites supported on TiO_2, SiO_2, and Al_2O_3 (0.45 to 9.5% dispersion) (Fig. 9a). Therefore, site–time yields are very similar on all monometallic Co catalysts ($1.6–3.0 \times 10^{-3}$ s^{-1}) (Fig. 9b). In this dispersion range, the chemical reactivity of surface Co atoms in the Fischer–Tropsch synthesis is not influenced strongly by Co crystallite size or by the chemical identity of the metal oxide support (*10, 35, 36*).

Apparently, volumetric Fischer–Tropsch synthesis rates on monometallic cobalt catalysts can be improved only by increasing the dispersion of supported cobalt crystals (i.e., the number of sites), because site reactivity is unaffected by catalyst modifications. Small crystals of Co oxide precursors, however, are difficult to reduce; also, they reoxidize easily during FT synthesis, leading to materials with low activity and high selectivity to methane and light hydrocarbons (*10, 36*). Thus, improved Co-based FT synthesis catalysts must not rely solely on the synthesis of smaller Co crystallites, but must also exploit bimetallic interactions that can improve the apparent site reactivity of exposed Co ensembles and the reducibility of dispersed Co oxide precursors. Small amounts of Ru introduce such desired effects into supported Co catalysts. As we discussed above, Ru increases the rate of reduction of highly dispersed CoO layers formed from glycol citrate precursors. In the next section, we describe Ru-promoted Co catalysts with Co-time yields significantly higher than expected from the data in Fig. 9. In effect, the presence of small amounts of Ru within Co crystallites increases the apparent reactivity of exposed Co atoms in FT synthesis reactions.

5.2. The Effects of Bimetallic Co–Ru Interactions on Reaction Rates

The addition of Ru to Co/TiO_2 samples (Ru/Co = 0.0067 at.) and the subsequent reduction of the bimetallic precursor in-

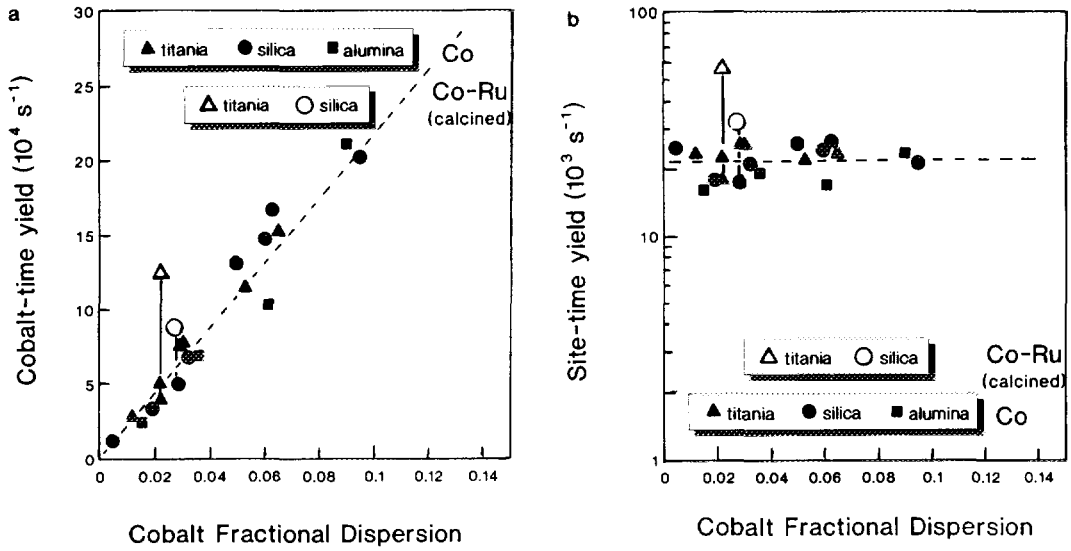

FIG. 9. Effects of cobalt dispersion and support on Fischer–Tropsch synthesis rates (473 K, H_2/CO = 2.1, 2000 kPa, 50–60% CO conversion): (a) metal–time yields and (b) site–time yields.

crease FT synthesis rates (Co–time yields) by a factor of two and the selectivity to C_5+ products from 84.5 to 86.2% (Table 5). Calcination of the bimetallic precursors for 1 h at 573 K before their reduction in hydrogen increases synthesis rates by an additional factor of two; C_5+ selectivities also increase further from 86.2 to 91.1%. These changes in catalytic behavior occur without any observable change in the Co dispersion when Ru is added to Co/TiO_2 (Table 3); therefore, the apparent site–time yields on Co-Ru samples is 2–4 times greater than on monometallic Co catalysts of identical dispersion (Table 5).

FT synthesis reactions on the Ru component of the bimetallic catalysts cannot account for the observed increase in reaction

TABLE 5

Bimetallic Synergy in Fischer–Tropsch Synthesis on $Co–Ru/TiO_2$ Catalysts

	Co	Co–Ru[a]	Co–Ru[a] (calcined)	Ru[d]
CO conversion	48.7	50.7	61.0	35.1
Metal–time yield[b] (10^4 s^{-1})	3.9	7.2	13.1	94.4
Cobalt–time yield[c] (10^4 s^{-1})	3.9	6.4	12.2	—
Site–time yield[c] (10^3 s^{-1})	17.7	29.1	55.5	16.3
CH_4 selectivity (%)	7.0	7.5	5.0	3.5
C_5+ selectivity (%)	84.5	86.2	91.1	93.0
Asymptotic chain growth probability	0.945	—	0.946	0.960

Note. Conditions: 473 K, 2000 kPa, H_2/Co = 2.05, 24 h on stream.

[a] 11.6% wt. Co; 0.14% wt. Ru; Ru/Co = 0.0067 at.

[b] Assuming no Ru contribution.

[c] After subtracting Ru contribution.

[d] 1.1% wt. Ru, 50% dispersion, TiO_2 support (*6*, *10*).

rate or C_5+ selectivity (Table 5). We can estimate the Ru contribution by using the observed Ru site-time yield on supported Ru catalysts (*10*) and by assuming that all of the added Ru is exposed to reactants and available for FT synthesis. We conclude that Ru sites contribute less than 10% of all FT synthesis products formed on calcined Co–Ru catalysts, not unexpected from the similar site-time yields on Ru and Co surface atoms and from the much higher concentration of the Co component in bimetallic samples (Table 5). The marked synergistic promotion of Co surface atoms by Ru remains even after the minor contribution of the Ru component is subtracted (Table 5).

The measured activation energies (88 ± 6 kJ mol^{-1}) and kinetic pressure orders (n = 0.60–0.65) for CO hydrogenation are similar on Co/TiO_2 and $Co–Ru/TiO_2$ catalysts, also suggesting that Ru does not affect the kinetic behavior of surface Co ensembles or contribute significantly to the observed FT synthesis products. Asymptotic chain growth probabilities, obtained from the linear part of Flory carbon number distribution plots (C_{15}–C_{50}) (*6*) are also identical on monometallic and Co–Ru bimetallic catalysts (a_∞ = 0.945; at 473 K, 2000 kPa, H_2/CO = 2.05); their value is lower than on Ru/TiO_2 catalysts at similar FT synthesis conditions (a_∞ = 0.960).

Bimetallic effects are strengthened by a calcination treatment that appears to induce more intimate contact between Co and Ru; the same treatment lowers the Co oxide reduction temperature and inhibits carbon deposition on bimetallic Co–Ru catalysts. These calcination treatments, however, did not affect the catalytic or chemisorptive properties of monometallic Co/TiO_2 samples.

We propose that the higher apparent site activity of Co–Ru catalysts reflects the ability of surface Ru atoms to maintain Co surfaces free of carbonaceous residues and of chemisorbed oxygen species during the initial few catalytic turnovers, when bare Co surface first contact H_2/CO reactants. Cobalt catalysts deactivate significantly during these first few turnovers, after which deactivation occurs much more slowly via the gradual formation of large surface chains and partially hydrogenated carbon species. The mode of bimetallic promotion that we propose here is consistent with the inhibition of carbon formation on Co–Ru catalysts and with the accelerating effect of Ru on the reduction of cobalt oxide precursors (Section 4.1). We cannot rule out that the observed bimetallic synergy arises from a direct effect of mixed Co–Ru ensembles on Fischer–Tropsch synthesis pathways. The higher apparent site reactivity but similar kinetics, however, suggest a higher site density, not different sites. Also, the lower surface carbon concentrations detected in TG (Section 4.1) and X-ray photoelectron spectroscopy studies (see the Appendix) are consistent with the inhibited deactivation model of Co–Ru bimetallic synergy.

The addition of Ru increases the apparent site reactivity of surface Co atoms. Indeed, cobalt- and site–time yields on Co–Ru samples lie above the extensive data set obtained for monometallic Co catalysts (Fig. 9), a significant improvement that we could not previously achieve through systematic variations of cobalt crystallite size or metal oxide support.

5.3. The Effects of Bimetallic Co–Ru Interactions on FT Synthesis Selectivity

The addition of Ru to Co/TiO_2 catalysts also increases the molecular weight (Fig. 10) and paraffin content (Fig. 11) of Fischer–Tropsch synthesis products. C_5+ selectivities increase with increasing bed residence time and with CO conversion on all catalysts (Fig. 10). Also, the olefin content of products decreases with increasing hydrocarbon chain size (Fig. 11).

Carbon number distributions do not obey Flory kinetics (i.e., $\alpha \neq$ constant) on Co or Co–Ru samples; the chain termination probability decreases with increasing chain

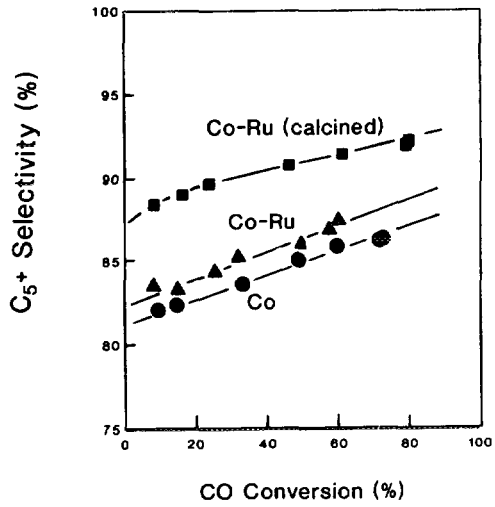

FIG. 10. C_5+ selectivity on Co/TiO_2 and $Co–Ru/TiO_2$ (Ru/Co = 0.0067 at.) catalysts (473 K, 2000 kPa, H_2/CO = 2.05; 11.6% wt. Co).

size (Fig. 12), suggesting that larger chains become increasingly difficult to terminate. Termination probabilities ultimately reach asymptotic values for chains larger than C_{15}. These asymptotic values are similar on Co and Co–Ru catalysts (Fig. 12); they are reached in the carbon number range where olefins no longer appear among FT synthesis products (Fig. 11). Chain termination probabilities for lighter hydrocarbons are higher on Co than on Co–Ru catalysts for all carbon numbers (Fig. 12).

These data are consistent with olefin readsorption pathways that occur during FT synthesis (*6–9*). Olefin desorption by hydrogen abstraction from surface alkyl chains is the predominant chain termination pathway in Co- and Ru-catalyzed FT synthesis (Scheme 1). This step can be reversed by the reattachment of reactive olefins to chain growth sites, where they continue to grow and from which they eventually desorb as higher molecular weight hydrocarbons. This readsorption process is enhanced by transport restrictions that selectively retain larger olefins and introduce concentration gradients within catalysts pellets; olefin readsorption is also enhanced by longer bed residence times in plug-flow reactors. Intrapellet transport restrictions worsen with increasing olefin size leading to a decrease in termination probability and in olefin content as chain size increases (Figs. 11 and 12) and also to the observed non-Flory carbon number distributions on Co and Ru catalysts (*6–10*).

5.4. The Role of Site Density and of Olefin Readsorption Pathways on FT Synthesis Selectivity

Experimental results and detailed models supporting the role of diffusion-enhanced readsorption of α-olefins in the control of FT synthesis selectivity have been previously described for Ru (*6–10*) and Co (*8–10*) catalysts. Selectivity changes caused by variations in metal dispersion or support reflect concurrent changes in pellet structure or site density, both of which influence the severity of transport restrictions, and not modifications of intrinsic chain growth or readsorption kinetics (*10*). In what follows, we show how the modifying effect of Ru on the C_5+ and paraffin selectivity of Co catalysts also reflects the transport-enhanced readsorption of α-olefins, a process favored at the

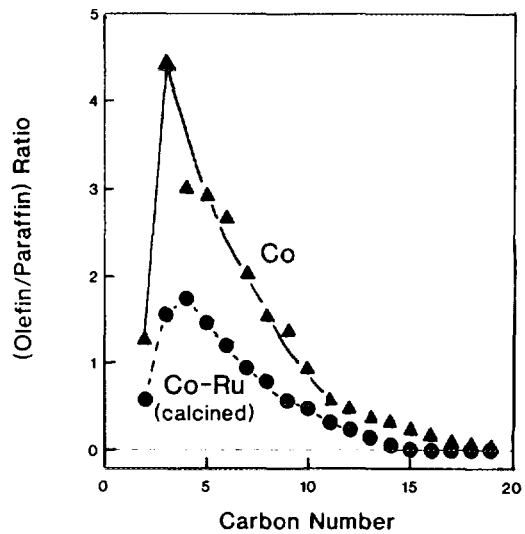

FIG. 11. Olefin-to-paraffin ratio on Co/TiO_2 and $Co–Ru/TiO_2$ (Ru/Co = 0.0067 at.) catalysts (473 K, 2000 kPa, H_2/CO = 2.05, 8–12% CO conversion).

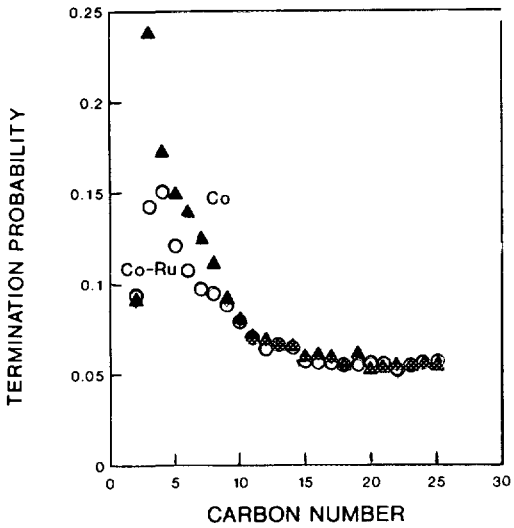

FIG. 12. Chain termination probability on Co/TiO_2 and $Co-Ru/TiO_2$ (Ru/Co = 0.0067 at.) catalysts (473 K, 2000 kPa, H_2/CO = 2.05, 8–12% CO conversion).

higher steady-state site density and volumetric rates obtained on bimetallic Co–Ru catalysts.

The residence time of α-olefins within catalysts pellets and the severity of intrapellet transport restrictions depend on the diffusive properties of reactive olefin molecules and on the structure of the porous support pellets. Intrapellet residence times increase with increasing pellet diameter (L) and decreasing support porosity (ε). Also, decreasing pore radius (r_p) worsens transport restrictions, even though intrinsic hydrocarbon diffusivities through liquid-filled pores do not depend on pore size. This occurs because for a given areal density of reactive sites (θ), smaller pores have a larger number of chain growth sites and lead to greater reactant consumption and product formation rates for a given cross-sectional pore area (through which molecules diffuse).

These structural properties arise naturally from a rigorous dimensional analysis of the reaction-transport equations required to describe this system (*6, 8, 9*). These treatments suggest that transport restrictions and the consequent enhancement of olefin readsorption pathways increase with increasing value of a structural parameter χ.

$$\chi = \frac{L^2 \cdot \varepsilon \cdot \theta}{r_p}.$$

Co–Ru catalysts resemble their monometallic counterparts in structural support properties. This structural parameter χ, however, also contains a measure of the density of active sites (θ), which determines the kinetic load that must be satisfied by transport in order to maintain uniform intrapellet concentrations of reactants and products. Steady-state site densities differ significantly between Co and Co–Ru catalysts; the higher Co–time yields on calcined Co–Ru catalysts suggest that steady-state site densities are about four times greater than on Co catalysts (Table 5). Thus, we expect that Co–Ru catalysts would be affected more strongly by transport-enhanced olefin readsorption processes because reaction rates are greater, whereas the pellet structural and transport properties required to satisfy these faster reaction rates are unaffected by the addition of Ru.

The C_5+ selectivity and the paraffin content on calcined $Co-Ru/TiO_2$ catalysts resemble those on other monometallic Co/TiO_2 samples containing higher site densities than those present on the Co/TiO_2 sample to which Ru was added (Fig. 13). Higher Co site densities, obtained by increasing the metal dispersion in Co/TiO_2 catalysts by a factor of about three, also increase C_5+ selectivities without an apparent change in site–time yields or in the chemical reactivity of exposed Co atoms (Fig. 13). Thus, the higher C_5+ selectivity and paraffin content observed on Co–Ru catalysts is consistent with their higher site density during steady-state Fischer–Tropsch synthesis catalysis. These effects do not arise from any chemical modification of surface cobalt ensembles or from any changes in intrinsic FT synthesis and readsorption kinetics caused by the presence of Ru atoms on the surface of Co crystallites.

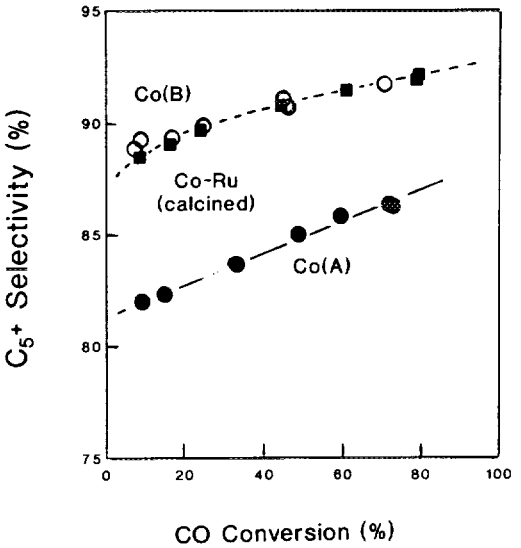

FIG. 13. C_5+ selectivity on Co/TiO_2 and $Co–Ru/TiO_2$ (Ru/Co = 0.0067 at.) catalysts (catalysts: Co (A), 11.6% wt. Co, 2.2% dispersion, 1.2 m g-atom surface Co/m^2 site density, TiO_2 support; Co (B), 12.1% wt. Co, 5.8% dispersion, 3.2 m g-atom surface Co/m^2 site density, TiO_2 support; Co–Ru, 11.6% wt. Co, 0.14% wt. Ru, 2.6% dispersion, TiO_2 support. (Conditions: 473 K, 2000 kPa, H_2/CO = 2.05.)

The enhanced readsorption of α-olefins on Co–Ru catalysts is also consistent with the lower chain termination probability (Fig. 12) and olefin content (Fig. 11) obtained on the bimetallic samples. In effect, Co–Ru samples reverse chain termination steps by readsorbing α-olefins more effectively in a process that selectively removes olefins and light hydrocarbons from the product stream.

5.5. *Regeneration of Deactivated Catalysts by Hydrogen Treatments*

Monometallic Co/TiO_2 catalysts deactivate at normal FT synthesis conditions (473 K, 2000 kPa, 25–50% CO conversion). Deactivation causes a decrease in product molecular weight and an increase in methane selectivity (Table 6). In part, these selectivity changes reflect the observed decrease in CO conversion as the catalyst deactivates, which lowers product molecular weight by decreasing secondary α-olefin readsorption reactions. The density of available Co sites decreases as deactivation proceeds, also weakening readsorption effects and decreasing product molecular weight. Deactivation occurs rapidly during the initial 1 h on stream; then, it slow down after 12–24 h to a steady-state deactivation rate corresponding to about a 20–30 day catalyst half-life. The deactivation of bimetallic Co–Ru samples is qualitatively similar to that occurring on Co catalysts. Steady-state deactivation rates are similar; thus, the retarding effect of Ru on carbon deposition reactions influences only the initial stages of deactivation, a process that occurs very rapidly during the initial equilibration of bare Co surfaces with synthesis gas.

A hydrogen treatment at reaction conditions (483 K, 14 h) did not restore initial Fischer–Tropsch synthesis rates or selectivities on monometallic Co catalysts supported on silica or titania (Table 6). On both calcined and uncalcined Co–Ru catalysts, however, this treatment restored rates and selectivities to values similar to those observed during the initial 24 h of catalyst operation (Table 6). Monometallic Ru catalysts can also be regenerated by contact with pure hydrogen streams at synthesis conditions, a property that we attribute to the presence of active sites for hydrogenation and hydrogenolysis of carbonaceous residues and of strongly chemisorbed oxygen.

Light hydrocarbons (C_1–C_7) are the predominant products of the hydrogen pretreatment of deactivated Co and Co–Ru catalysts. The initial rate of hydrocarbon formation is much higher on bimetallic catalysts, consistent with the presence of Ru ensembles on the surface of Co crystallites. On Co–Ru catalysts, hydrocarbon concentrations in the effluent hydrogen stream decrease to undetectable levels in 2–3 h. In contrast, hydrocarbons remain in the effluent after contacting monometallic Co catalysts with hydrogen for 12–16 h because hydrogenolysis rates are much slower in the absence of Ru.

TABLE 6

Deactivation and Regeneration Behavior of Co/TiO_2 and $Co-Ru/TiO_2$ Catalysts

	Cobalt-time yield (10^4 s^{-1})	Methane selectivity (%)	C_5+ selectivity
	Catalyst: Co/TiO_2		
Initial[a]	3.9	7.0	84.5
Before H_2 treatment[b]	2.4	8.3	81.5
After H_2 treatment[a]	2.6	8.1	82.0
	Catalyst: $Co-Ru/TiO_2$ (calcined)		
Initial[a]	13.2	5.0	91.1
Before H_2 treatment[b]	10.5	6.4	88.8
After H_2 treatment[a]	13.1	4.9	91.5

Note. Conditions: 473 K, 2000 kPa, H_2/CO = 2.05, 50–60% CO conversion.
[a] 24 h on stream after initial startup or regeneration treatment.
[b] H_2 treatment at 483–493 K, 100 kPa, 16 h, after 80–130 h on stream.

The rate of hexadecane hydrogenolysis in the presence of pure H_2 is more than ten times faster on Ru than on Co catalysts (Fig. 14). The addition of Ru to Co/SiO_2 catalysts increases hydrogenolysis site-time yields by a factor of 6 to 7, suggesting again that a significant fraction of the added Ru is exposed at the surface and available to catalyze hydrogenolysis reactions of large hydrocarbons during both C_{16} hydrogenolysis and catalyst rejuvenation. C_{16} reacts predominantly by sequential cleavage of terminal carbons on both Co and Ru catalysts. The molar fraction of methane among hydrogenolysis products is greater than 0.90. Hexadecane hydrogenolysis product resemble those observed during hydrogen pretreatment of deactivated catalysts, where methane is also the predominant reaction product. The presence of small amounts of CO in the hydrogen feed (20 kPa) strongly inhibits both C_{16} and wax hydrogenolysis rates on all catalysts.

5.6. *Bimetallic Synergy in SiO_2-Supported Co–Ru Catalysts*

The bimetallic synergy occurring on TiO_2-supported Co–Ru catalysts is also observed when similar crystallites are supported on SiO_2. On silica supports, the addition of Ru (0.26% wt. Ru, Ru/Co = 0.007 at.) increases cobalt-time yields by almost a factor of two (Table 7), without increasing the cobalt dispersion measured by hydrogen chemisorp-

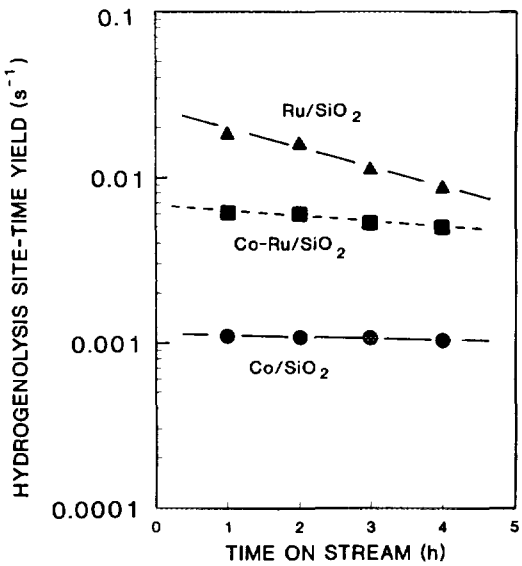

FIG. 14. Hexadecane hydrogenolysis site–time yields on SiO_2-supported Co, Ru, and Co–Ru catalysts (conditions: 493 K for Co and Co–Ru, 473 K for Ru, 800 kPa H_2. Catalysts: Co/SiO_2, 23% wt. Co, 2.85% dispersion; Co–Ru, 23% wt. Co, 0.26% wt. Ru, 2.73% total exposed metal; Ru, 10.8% wt., 20.8% dispersion).

TABLE 7

Fischer–Tropsch Synthesis on Co/SiO_2 and $CoRu/SiO_2$ Catalysts

Catalyst	Co/SiO_2	$CoRu/SiO_2$[a] (calcined)
Cobalt-time yield (10^4 s^{-1})	5.0	8.4
Site-time yield (10^3 s^{-1})	17.5	32.0
CH_4 selectivity (%)	6.5	5.8
C_5+ selectivity (%)	82.0	86.1
Chemisorption uptake (H/CO)	0.0285	0.0273

Note. Conditions: 2060 kPa, 200°C, H_2/CO = 2/1, 55–63% CO conversion.

[a] 23% wt. Co, 0.26% wt. Ru.

tion (Table 2) or electron microscopy and without changing the reaction activation energy or kinetic pressure dependence. C_5+ selectivity increased from 82.0 to 86.1% with Ru addition. A calcination treatment was required to induce the observed bimetallic synergy, an effect that also appears to require intimate mixing between the two metal components on SiO_2 supports. Thermogravimetric measurements suggest that similar calcination treatments (573 K) also increase the rate of reduction of Co oxide precursors supported on silica (Fig. 4).

5.7. Comparisons with Literature Reports on Co–Ru FT Synthesis Catalysts

The only other extensive study of Co–Ru catalysts for the Fischer–Tropsch synthesis was described in a series of U.S. patents assigned to Gulf (*13–16*). These samples were prepared by impregnating alumina with Co nitrate, drying, and introducing Ru and thoria as catalyst promoters. The initial reports disclosed catalysts directly reduced after Ru impregnation (catalyst A, Table 2); their Co-time yields and C_5+ selectivities were much lower than those on the Co–Ru samples of our study (Table 2). Co oxide precursors supported on alumina are very difficult to reduce completely to Co metal (*36*), especially at the low reduction temperatures used in these studies (623–633 K). As a result, it is difficult to conclude whether the observed synergy arises from the more facile reduction of these precursors in the presence of Ru or from any unique catalytic properties of Ru-promoted surfaces.

Two later patents describe the benefit of a reduction–oxidation–reduction (ROR) treatment on monometallic Co (*16*) and on bimetallic Co–Ru (*13*) catalysts supported on alumina. Reaction rates increase by about a factor of two when reduced samples undergo an additional oxidation–reduction treatment (*13*) even at (Co/Ru) atomic ratios as high as about 700 (catalyst B, Table 2). These effects were also observed on monometallic Co catalysts supported on alumina, suggesting that the observed calcination effects do not arise from a more intimate mixing between Co and Ru but from either the removal of impurities or from the formation of more reducible monometallic Co oxide crystallites during the ROR treatment. We have examined the effect of Ru and of calcination treatments only on fully reduced Co catalysts supported on titania and silica. In our study, the calcination treatments did not affect the catalytic behavior of monometallic Co catalysts. Our data suggest that neither surface impurities nor enhanced reduction account for the calcination effects on reaction rate and selectivity that we have observed in our study.

6. CONCLUSIONS

CO hydrogenation and olefin readsorption kinetics are unaffected by the presence of small amounts of Ru in supported Co catalysts. Cobalt dispersion is not influenced by the presence of Ru or by the calcination treatment required to induce intimate bimetallic mixing. Thus, neither the reaction pathways nor the initial density of Co surface atoms appear to be affected by Ru. We suggest that the observed improvement in site–time yield and C_5+ selectivity arises instead from the higher stability of mixed Co–Ru ensembles against deactivation during initial FT synthesis turnovers.

The higher apparent site–time yields on Co–Ru catalysts reflect the larger number

of exposed Co atoms available for catalytic turnovers during FT synthesis. The higher selectivity to C_5+ hydrocarbons and the higher paraffin content in the products is caused by enhanced readsorption of α-olefins, a process favored by transport restrictions that become more severe at the higher density of active sites available in the bimetallic catalysts.

In the absence of CO, surface Ru atoms catalyze hydrogenolysis reactions of paraffins at Fischer–Tropsch synthesis temperatures, a property that permits the regeneration of Ru-based Fischer–Tropsch catalysts by a simple hydrogen treatment at reaction temperatures. The presence of trace amounts of Ru (Ru/Co = 0.0067 at.) imparts this desirable property to supported Co catalysts. The catalytic effect of Ru on the hydrogenolysis of carbonaceous deposits and on the reduction of surface oxygen during CO hydrogenation may also account for the apparent inhibition of carbon deposition in H_2/CO mixtures and for the protection of Co surface ensembles against deactivation during catalysis.

APPENDIX: X-RAY PHOTOELECTRON SPECTRA OF Ru-DOPED Co FOILS

X-ray photoelectron spectra were obtained using a PHI Model 5300 (Perkin–Elmer) spectrometer placed within an ultrahigh vacuum (UHV). This chamber is equipped with a sample manipulator and an environmental chamber, where samples could be pretreated and transferred to the UHV chamber without exposure to air. Data were obtained using Mg-$K\alpha$ radiation and a hemispherical analyzer. The elemental composition of near-surface layers were obtained from the intensities of the Co ($2p_{1/2,3/2}$) and the Ru ($3d_{3/2,5/2}$) XPS peaks, normalized by their intensity in pure Co and Ru samples. Samples were prepared by impregnating a Co foil (99.999% purity) with a Ru nitrate/acetone solution, followed by drying at room temperature. This sample was subjected to sequential reduction (773 K, 4% H_2/He) and oxidation (573 K, 2% O_2/He) treatments. XPS spectra were obtained after each of these treatments by transferring the samples between the pretreatment cell and the UHV chamber without exposing samples to air. The carbon content in near-surface layers after Fischer–Tropsch synthesis at various temperatures (473–773 K, 100 kPa, H_2/CO = 2.0) was measured from the relative intensity of the C (1s) and Co XPS peaks.

Co foils impregnated with Ru and reduced in hydrogen initially contained similar amounts of Co and Ru within surface layers. Calcination of these foils decreases markedly the surface concentration of Ru, suggesting extensive migration of Ru atoms into the bulk of the Co foil (Fig. A1). This is consistent with the expected miscibility of Co and Ru oxides. These data are also consistent with the intimate mixing that we have proposed to explain the marked effect of calcination on the reduction, carburization and catalytic properties of Co–Ru samples.

A subsequent reduction of oxidized samples returns a significant fraction of the Ru atoms to near-surface regions (Fig. A1), as expected from the limited solubility of

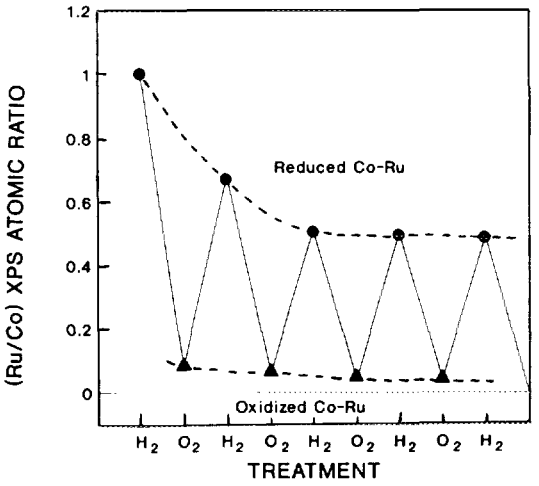

FIG. A1. The effect of reduction (4% H_2/He, 773 K) and calcination (2% O_2/He, 573 K) treatments on the ratio of the Ru ($3d_{3/2,5/2}$) and Co ($2p_{1/2,3/2}$) XPS peak intensities on Ru-promoted Co foils.

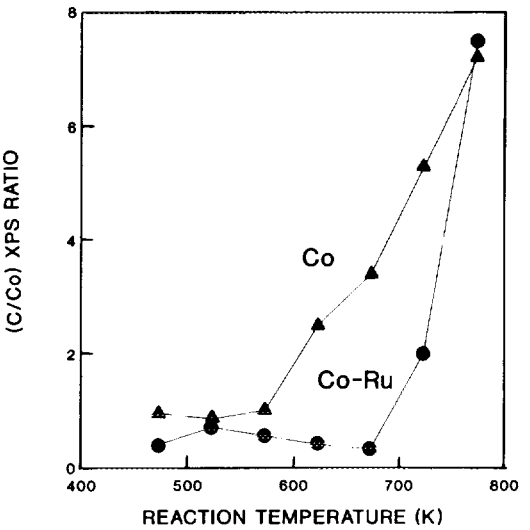

FIG. A2. Carbon deposition from H_2/CO mixtures (101 kPa, H_2/CO = 2) on Co and Co–Ru foils. The effect of reaction temperature on the ratio of C(1*s*) to Co($2p_{1/2,3/2}$) XPS peak intensities.

Co–Ru alloys. Ru appears to reside preferentially at the surface of such alloys but not all deposited Ru returns to the surface after a reduction treatment, suggesting that some bulk mixing of the two metallic components occurs. The surface segregation of the Ru component after reduction is confirmed by a marked increase in Ru/Co intensity ratios observed as we approach glancing photoelectron take-off angles. As we observed also on supported Co–Ru samples, calcination induces intimate mixing between the two metals in Co–Ru foils, and a subsequent reduction returns a large fraction of the Ru atoms to the surface of large Co crystallites.

The deposition of carbon occurs rapidly above 600 K when Co foils are contacted with H_2/CO mixtures, as shown by the rapid increase in C/Co XPS intensity ratios with increasing exposure temperature (Fig. A2). Reduced Ru-promoted Co foils resemble pure Co foils in their carbon deposition properties. Apparently the Ru component is initially present in very large crystallites and in poor contact with the underlying Co surface. Calcination-reduction treatments of these samples, however, strongly inhibit carbon deposition rates (Fig. A2); carbon formation then requires significantly higher temperatures (100–150 K) on Co–Ru than on pure Co foils. The large C/Co XPS intensity ratios observed above 750 K on all samples suggest the formation of several carbon monolayers, consistent with the carbon whiskers observed in electron microscopy studies of supported Co catalysts.

C/Co XPS intensity ratios are slightly lower on Co–Ru than on Co foils when samples are exposed to H_2/CO mixtures at normal Fischer–Tropsch synthesis temperatures (473–523 K) (Fig. A2). These data are consistent with the proposed cleansing effect of Ru on Co surfaces and with the apparently higher density of Co sites available during catalysis when Co and Ru are intimately mixed on crystallite surfaces.

ACKNOWLEDGMENTS

We thank Messrs. B. A. DeRites and S. Miseo and Mrs. H. Vroman for their expert technical assistance in conducting these experiments. We also thank Dr. G. B. Ansell for the X-ray diffraction data, Dr. K. S. Kim for the X-ray photoelectron spectra, and Dr. E. B. Prestridge for the electron microscopy studies. Finally, we acknowledge Dr. J. H. Sinfelt and the late Professor P. Biloen (University of Pittsburgh) for helpful discussions on the catalytic chemistry of bimetallic materials. The XAFS measurements were performed at the Stanford Synchrotron Radiation Laboratory, a facility supported by the U.S. Department of Energy.

REFERENCES

1. Storch, H. H., Golumbic, N., and Anderson, R. B., "Fischer–Tropsch and Related Syntheses." Wiley, New York, 1951.
2. Pichler, H., *Adv. Catal.* **4,** 271, (1952).
3. Anderson, R. B., *in* "Catalysis" (P. H. Emmett, Ed.). Rheinhold, New York, 1959.
4. Fischer, F., and Tropsch, H., *Brennst. Chem.* **13,** 61 (1932).
5. Flory, P. J., *J. Am. Chem. Soc.* **58,** 1877 (1936).
6. Iglesia, E., Reyes, S. C., and Madon, R. J., *J. Catal.* **129,** 238 (1991).
7. Madon, R. J., Iglesia, E., and Reyes, S. C., *J. Phys. Chem.* **95,** 7795 (1991).
8. Iglesia, E., Reyes, S. C., and Soled, S. L., *in* "Computer Aided Design of Catalysts" (E. R. Becker and C. J. Pereira, Eds.). Dekker, New York, 1992.
9. Iglesia, E., Reyes, S. C., Soled, S. L., and Madon, R. J., *in* "Advances in Catalysis and Related Sub-

jects" (D. D. Eley, P. B. Weisz, and H. Pines, Eds.), Vol. 39, p. 221. Academic Press, San Diego, 1993.
10. Iglesia, E., Soled, S. L., and Fiato, R. A., *J. Catal.* **137,** 212 (1992).
11. Schwab, G. M., *in* "Catalysis Science and Technology" J. R. Anderson and M. Boudart, Vol. 2, Chap. 1. Springer-Verlag, New York, 1981.
12. Carter, J. L., McVicker, G. B. Weissman, W., Kmak, W. S., and Sinfelt, J. H., *Appl. Catal.* **3,** 327 (1982).
13. Beuther, H., Kobylinski, T. P., Kibby, C. L., and Pannell, R. B., U.S. Patent 4,585,798 (1986), assigned to Gulf Research and Development Co.
14. Beuther, H., Kibby, C. L., Kobylinski, T. P., and Pannell, R. B., U.S. Patent 4,413,064 (1983), assigned to Gulf Research and Development Co.
15. Beuther, H., Kibby, C. L., Kobylinski, T. P., and Pannell, R. B., U.S. Patent 4,493,905 (1985), assigned to Gulf Research and Development Co.
16. Kobylinski, T. P., Kibby, C. L., Pannell, R. B., and Eddy, E. L., U.S. Patent 4,605,676 (1986), assigned to Chevron Research Co.
17. Nowack, G. P., Johnson, M. M., and Tabler, D. C., U.S. Patent 4,394,298 (1983), assigned to Phillips Petroleum Co.
18. Knifton, J. F., and Lin, J. J., U.S. Patent 4,366,259 (1982), assigned to Texaco, Inc.
19. Iglesia, E., Soled, S. L., and Fiato, R. A., U.S. Patent 4,738,948 (1988), assigned to Exxon Research and Engineering Co.
20. Iglesia, E., Soled, S. L., and Fiato, R. A., U.S. Patent 4,822,824 (1989), assigned to Exxon Research and Engineering Co.
21. Prestridge, E. B., and Yates, D. J. C., *Nature* **234,** 345 (1971).
22. Lyttle, F. W., Greegor, R. B., Marques, E. C., Sandstrom, D. R., Via, G. H., and Sinfelt, J. H., *J. Catal.* **95,** 546 (1985).
23. Stern, E. A., and Heald, S. M., *Nucl. Instrum. Methods* **172,** 397 (1980).
24. Via, G. H., Sinfelt, J. H., and Lyttle, F. W., *J. Chem. Phys.* **71,** 690 (1979).
25. Via, G. H., Drake, K. F., Meitzner, G. D., Lyttle, F. W., and Sinfelt, J. H., *Catal. Lett.* **5,** 25 (1990).
26. Teo, B. K., and Lee, P. A., *J. Am. Chem. Soc.* **101,** 2815 (1979).
27. Klug, H. P., and Alexander, L. E., "X-ray Diffraction Procedures." Wiley, New York, 1954.
28. Flory, P. J., *J. Am. Chem. Soc.* **58,** 1877 (1936).
29. Friedel, R. A., and Anderson, R. B., *J. Am. Chem. Soc.* **72,** 1212 (1950).
30. Baker, R. T. K., Barber, M. A., Harris, P. S., Feates, F. S., and Waite, R. J., *J. Catal.* **26,** 51 (1972).
31. Dulac, J., *Bull. Soc. Fr. Mineral. Cristallogr.* **92,** 487 (1969).
32. Tauster, S. J., Fung, S. C., Baker, R. T. K., and Horsley, J. A., *Science* **211,** 1121 (1981).
33. Soled, S. L., and Iglesia, E., unpublished results.
34. Bartholomew, C. H., and Farrauto, R. J., *J. Catal.* **45,** 41 (1976).
35. Ho, S. W., Houalla, M., and Hercules, D. M., *J. Phys. Chem.* **94,** 6396 (1990).
36. Johnson, B. G., Bartholomew, C. H., and Goodman, D. W., *J. Catal.* **128,** 231 (1991).
37. Koelbel, H., and Engelhardt, F., *Erdoel Kohle* **2,** 52 (1949).
38. Blanchard, M., and Bonnet, R., *Bull. Soc. Chim. Fr.* **1–2,** 7 (1977).
39. Reuel, R. C., and Bartholomew, C. H., *J. Catal.* **85,** 78 (1984).
40. Great Britain Patent 2,130,113A (1984), assigned to Shell Research and Development.